INTERNATIONAL JOURNAL OF Telecommunications
AIR DEFENSE COLLEGE

Design and Implementation of High-Power Fiber Laser Chamber Test Under Different Aerosols Conditions

Abdalrhman Adel [1], Amir Almslmany [2*], Mohamed Mabrouk [3], Mohamed Shehata [4], Mohammed Alamir [5], and Mostafa Alshershby [6]

Citation: Adel, A.; Almslmany, A.; Mabrouk, M.; Shehata, M.; Alamir, M.; Alshershby, M. *International Journal of Telecommunications,* ***IJT'2021****, Vol. 01, Issue 01, pp. 1-15, December 2021.* https://ijt-adc.org/articles/2805-3044/704131

Editor-in-Chief: Yasser M. Madany
Received: 30-10-2021
Accepted: 15-12-2021
Published: 19-12-2021

Publisher's Note: The International Journal of Telecommunications, IJT, stays neutral regarding jurisdictional claims in published maps and institutional affiliations.

[1] Dept. of Electronics & Comm., Egyptian Air Defense College; abdou40105@gmail.com
[2] Dept. of Electronics & Comm., Egyptian Air Defense College; dr.mslmany.7256.adc@alexu.edu.eg
[3] Dept. of Electronics & Comm., Faculty of Engineering, Alexandria Univ.; 3mmabr084@uottawa.ca
[4] Dept. of Electronics & Comm., Egyptian Air Defense College; mohamed_elhadad@ymail.com
[5] Alexandria Higher Institute Engineering & Technology AIET; dr.mohammed.alamir@aiet.edu.eg
[6] Dept. of Electronics & Comm., Egyptian Air Defense College; m_alshershaby@yahoo.com
* Correspondence: dr.mslmany.7256.adc@alexu.edu.eg; Tel.: (+20-01120000739)

Abstract: In the past two decades, the important role of high-energy lasers (HEL) has emerged in various civilian and military fields. Therefore, foundations and theories of high-power laser radiation have been developed to serve these applications, including the high-power laser aerosol test chamber. This room simulates different weather conditions in a clear and misty atmosphere. In applications that operate at long range, for example, high-energy laser weapons are used to secure an important area against guided bombs. Changes in climatic conditions are an important and influencing factor in the method of high-energy laser radiation, so atmospheric conditions such as industrial weather had to be simulated in the test room. In this paper the interaction between laser beam and different metals such as stainless steel and aluminum was measured with accurate values of heat capacity (HC) at 1.4 J\C and melting point (MP) by temperature 600C and 1000C respectively reached in the presence of different types of aerosols with real experiments in order to simulate weather conditions in the far field. These experiments were conducted in a High Energy Laser Chamber Test (HELCT) that was previously designed and implemented by the authors.

Keywords: Atmospheric aerosol; HEL; HELCT; HC; MP.

1. Introduction

Recently, the study of the behavior of light propagation, and the interaction of light with the material of the medium is considered one of the most important branches of modern applied light [1], as many different optical phenomena appear when the light ray passes through aerosols materials, specifically, absorption negativity, scattering, polarization, and electro-optical and magnetic phenomena that can be understood using basic rules. When a beam of laser passes through a substance in its condition of matter, its prevalence impacted on both sides' important ways firstly, the intensity will always decrease to an extent whose amount varies When light passes far into the center and secondly, the speed in the center will be slower than its counterpart in space. Absorption is the primary cause of the drop in intensity; however, Scattering may also be essential in some situations [2].

General selective absorption and transmission When the intensity of light at all wavelengths is diminished, a medium is said to exhibit universal absorption. The same quantitative amount. And the rate of light after it goes out as seen by the eye Does not give noticeable color. There is only a lack of intensity the likes of this appear

gray matter. equally. However, some of them are in common, such as a suspension of black soot or thin translucent slices of Platinum 'approaches this condition in a wide range of wavelengths. Absorption means absorption of certain baggage of light without other. The colors of practically all pigments are due to absorption.
Or some. visible light spectrum So, a sliver of lime-green acrylic absorbs both ends Red and blue are the spectrum, and the rest of the light transmits to the eye, giving the eye a sense of color the green. Selective absorption is responsible for the colors found in most natural objects like paintings, flowers, and so on. It is said that these objects are dyed or colored in the body, which distinguishes them from the color of the surface because its color results from the light that penetrates to a certain distance through the material. Then because of scattering or reflection, deflected or emitted from the surface. but after it travels a certain distance in the middle during which the colors that are selectively absorbed are taken away. And in like this for all conditions the absorption of the body will be directly proportional to the internal absorption, and it will stop the same method on the wavelength. On the other hand, the surface color is produced by the process for reflection at the same surface. And to hate the material and in particular the minerals Like gold or copper, it has a higher reflective strength for some colors than for others They get their color from reflected light.

2. Methodology of the Creating (HPL) Chamber Test

There are two lenses within the chamber holder for the chamber test: one is used to maintain the laser beam exit deviation angle, and the other is used to measure how far the beam deviates from the target. giving it nearly 0.75 mrad. Inside the chamber test holder, a laser point diameter of 30 cm was achieved [11]. The second negative Plano-convex lens focuses the laser beam at a specific focus depending on the power meters' sensor area [12]. Consequently, the power meter does not reach saturation. The first lens is manufactured of zinc sliend with a thickness of 8.44 cm and front and back radii of 118.9 mm and 91.961 cm, respectively, for creating Plano-convex lenses. The second lens is constructed of zinc sliend and has front and back radii of 52.3 cm and 32.651 cm, respectively. The 2D HEL chamber test is shown in figure 1 Inside the chamber test, Figure 2 illustrates the 2D positive and negative lenses.

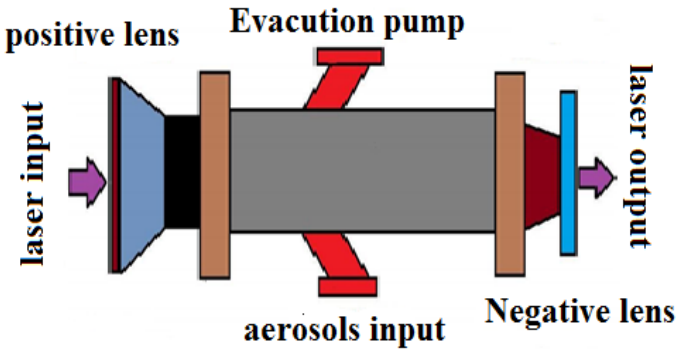

Figure 1. The 2D HEL chamber test.

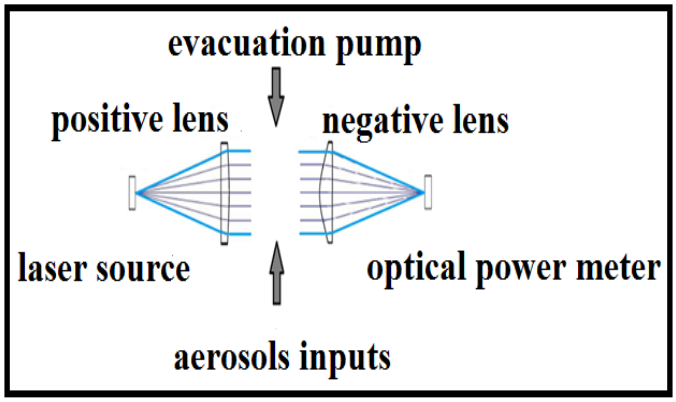

Figure 2. the 2D positive and negative lenses inside the HEL chamber test.

2.1. Study case of a laser beam inside a smoke-filled tube

Figure 3 depicts a long metal cylinder filled with paint black that is open to light of intensity I_0. The window beam's intensity will be set at a specific level. However, it's less than I_0, which is good news. Experimentation reveals that for a given smoke density, I is dependent on cylinder length D and kind of smoke, as shown by equation 1.

$$I = I_0 e^{-\alpha d} \quad (1)$$

α Absorption coefficient is a term used to describe the pace at which light from a direct beam dim. In this scenario, the fall in intensity from 3 to 1 is primarily due to the absence of the Real light, but it is not included in the direct package because Dust particles scatter some of the light. Even with highly diluted smoke, it's still effective.

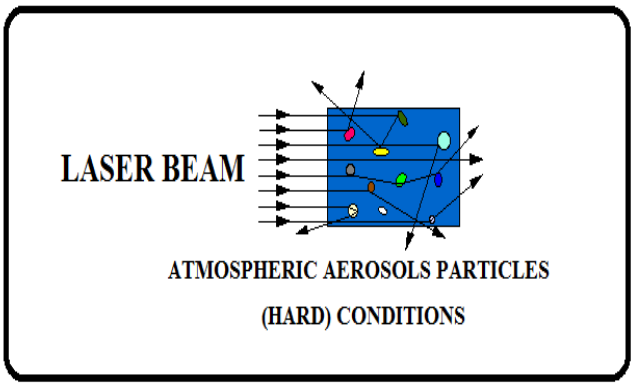

Figure 3. Laser beam pathing through a hard-atmospheric particle.

An easy way to determine the intensity of scattered light is to look at the tube from the side in a darkened environment. Minutes floating in the air allow the sun to look past walls and into rooms.
The absence of light is what is meant by true absorption. whose motion is created by converting energy into motion Particles that are good at absorbing heat. This will only happen to a small extent in previous experience. In figure 4. The average particle diameter of atmospheric aerosols and the number of con centration in a proposed chamber test.

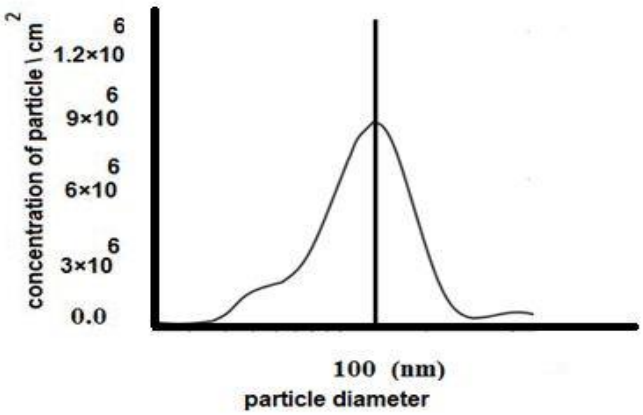

Figure 4. Relation between the average particle number and concentration per cm^2in proposed system.

In this graph, it shows that the average diameter of the suspended particles in the chamber test is 100 nanometers and with an average concentration 9×10^6 These values are among the best values that put a high-powered laser beam in a near-real test in difficult weather conditions. On the other hand, the equivalent concentration for good weather conditions inside the chamber test is 3×10^6.

2.2. Absorption by solids and liquids

Because of absorption, when monochromatic light travels through a solid or liquid in a transparent cell, the transmitted light's intensity is substantially lower than the incident lights. The wavelength of the incident light can be altered if as the absorption changes, so does the amount that is absorbed. Absorption may be measured simultaneously over a wide range of wavelengths using a simple technique.

Making the light from the source 'parallel' through the lens is a typical way to demonstrate this action. To cut the absorbent material to a specific thickness. Then use another lens to picture thin film in figure 5 after passing through the substance and finally transparent from prism. After this process, the effect of monochromatic light on the photographic film is studied in terms of power and beam shape, is it homogeneous or heterogeneous, and so on.

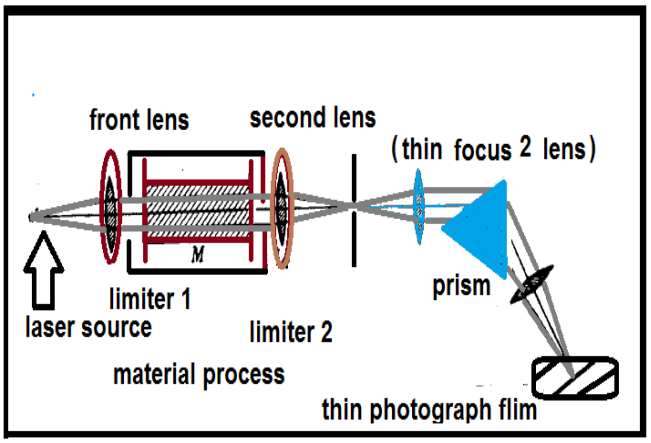

Figure 5. A classical method to be study the effect of absorption by liquid and solid.

Many atmospheric light propagation problems necessitate knowledge of both the energetic losses and the angular distribution of the energy sucked out of a beam in addition to the former. Laser sounding problems, high-level detection and range problems, as well as many others might be brought up in connection [16].

Polydisperse ensembles of spherical particles can readily have their scattering phase functions determined. There is a great deal of calculated information about this function elsewhere in. varied wavelengths and sets of microstructure characteristics in the literature [18]. The He-Ne laser, the Nd–yag laser and the CO_2 laser show some results of calculations for fog and clouds in Figure 6.

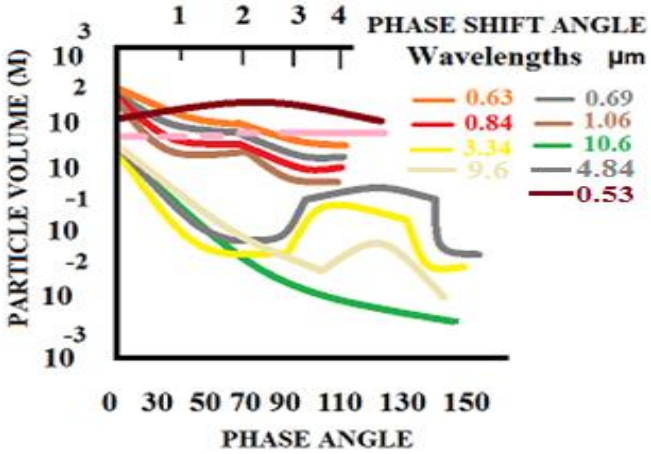

Figure 6. Scattering phase function of water clouds and fogs for gamma-distribution.

For example, there is the CO_2 laser with an output wavelength of 10.6 microns, the ruby laser with an output wavelength of 0.69 microns, and lasers made of Nd Yag with an output wavelength of 1.06 micrometers for fogs and clouds with gamma size-distribution functions, Figure 6 illustrates the derived data [19].

According to this diagram, water clouds' scattering phase functions are very smooth. As a result, fogs and clouds scatter light in a highly asymmetrical way. In this situation, the forward-scattered radiation flux dwarfs the backward-scattered radiation flux by a factor of three to five. To put this in perspective, the amplitude of hazes is around two to three orders of magnitude higher.

Several experimental results on measuring the scattering phase functions of atmospheric aerosols are included in the monograph. These findings are qualitatively in line with what was previously computed. The absence of data on aerosol microphysical characteristics makes it difficult to conduct a quantitative comparison. In addition, all measurements of the aerosol scattering phase functions were carried out within the visible spectrum of electromagnetic radiation [22].

2.3. Size distribution of aerosol particles and fog droplets (FDSD)

In the atmosphere, there exist several distribution models. For the most part, the various sizes of a particle group are represented using the aerosol number size distribution. Several lognormal distributions may be used to explain APSD in general. The following equations describe it perfectly.

$$n(r) = \sum_{i=1}^{k} \frac{N_i}{\sqrt{2\pi} \cdot \ln \sigma_i \cdot r} \exp\left(-\frac{(\ln r - \ln r_{mi}^n)^2}{2(\ln \sigma_i)^2}\right), \qquad k = 1,2, \ldots \tag{2}$$

n(r) indicates the number concentration distribution, k the number of modes, and Ni the total particle number of the (i) mode. The radius (r_{mi}^n) and width ($ln\ \sigma_i^2$) are described by the number concentration distribution and APSD, respectively.

Atmospheric aerosols may often be divided into four categories, based on their source: urban industrial or biomass burning aerosols, desert dust, or marine origin aerosol. Volume concentration distribution v(r) can be expressed with the same distribution, which is preferable since fine and coarse modes of volume concentration representation are easily distinguishable [24]. With respect to n(r) and v(r), there is no difference in the standard deviation between the two functions. Table 1 lists the characteristics for these common aerosols, and Figure 7 shows how extinction efficacy varies with particle size, with a progressive increase [25].

Table 1. Types of Aerosol Bimodal Distribution: Typical Parameters.

Parameter for Aerosol Particle Size	Industrialized cities	Using Biomass as a Fuel	Oceanic and Saharan Dust
r_{m1}(μm)	(0.14)-(0.18)	(0.13-0.16)	(0.12-0.16)
r_{m2}(μm)	(2.70)-(3.20)	(3.20-3.70)	(1.90-2.70)
ln σ_1	(0.38)-(0.46)	(0.40-0.47)	(0.40-0.53)
ln σ_2	(0.60)-(0.80)	(0.70-0.80)	(0.60-0.70)
V1/V2	(0.80)-(2.00)	(1.30-2.50)	(0.10-0.50)
m_r	(1.40)-(1.47)	(1.47-1.52)	(1.36-1.56)

It is important to note that extinction efficiency maximum peak diameters vary with wavelength. Extinction coefficient, on the other hand, can provide a more accurate picture of particle size distribution in this location Extinction at longer wavelengths allows for the identification of big particles. However, obtaining and detecting mid-infrared or longer-band beams of light is difficult. In order to identify big airborne particles, we suggest using small-angle forward scattering coefficients in conjunction with extinction coefficients [26].

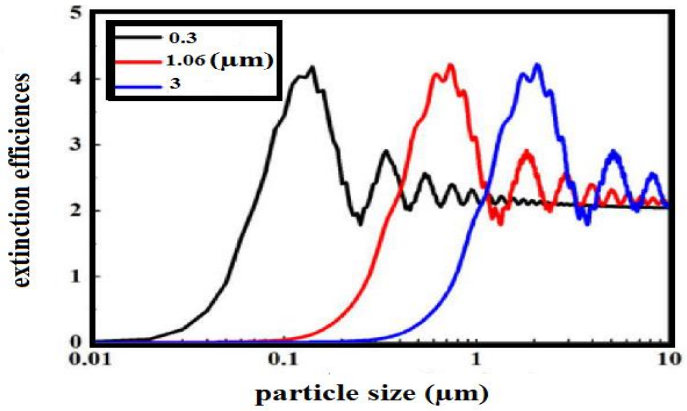

Figure 7. Extinction efficiencies 0.3,3μ m and 1.06μ m wavelengths.

Figure 8 depicts the scattering phase function of a particle with a λ (0.3μm, 0.55 μm, and 1.06 μm) with a refractive index of 1.50-0.01 varying with the angle of incidence. Fig. 7 shows the scattering peak's greatest value. In comparison to extinction efficiency, phase function is better at capturing the properties of big particles.

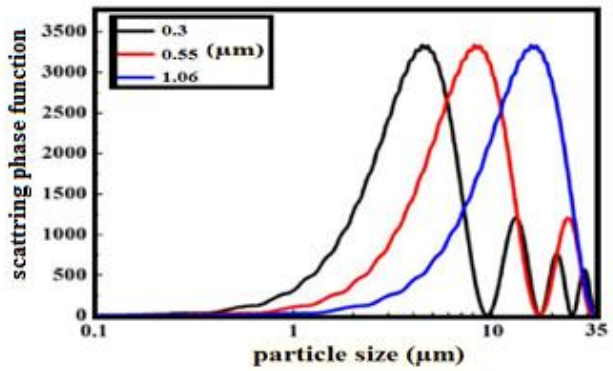

Figure 8. Wavelength, angle, and scattering phase function at three wavelengths and four angles: wavelength 0. 55 micrometers, and 1.06 micrometers.

3. Chamber test implementation step-by-step guide

Optical subsystem design and analysis for the aberration parameters optical sub system were proposed in this part, as was hardware implementation. Implementation of a two-lens Plano convex system in the first stage Following the ray tracing process, the lens scale is shown in Figures (9–10).

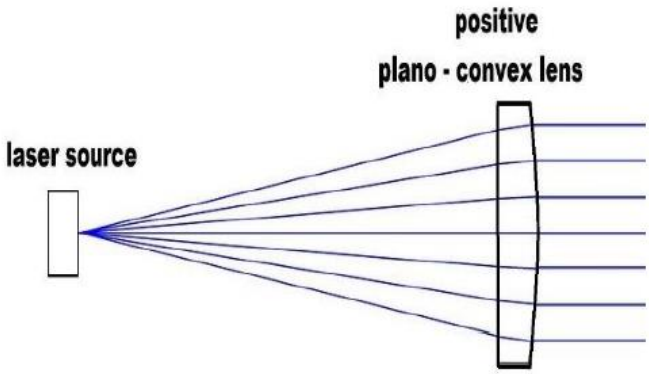

Figure 9. Positive Plano-Convex Lens Design with Ray Trace.

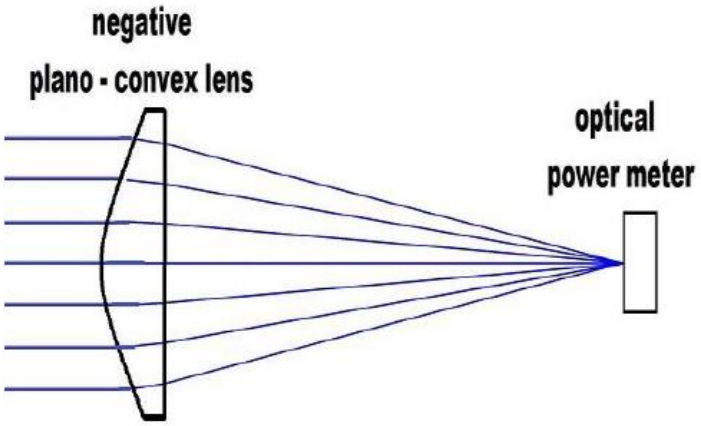

Figure 10. Negative Plano-Convex Lens Design with Ray Trace.

In the second stage, a 3D-scale lens cure is used to accurately measure the lens's parameters using 3D optics software such as Win Lens and optocad. as seen in Figures 11, 12, and 13.

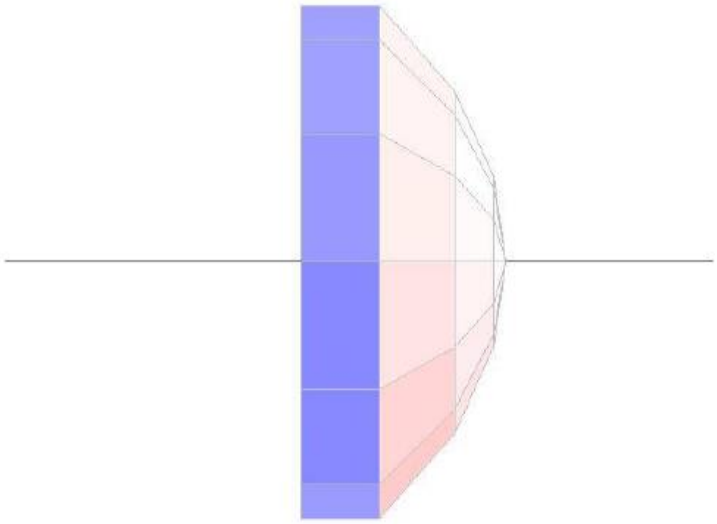

Figure 11. Positivistic ally curved plano-convex lens designed in 3D.

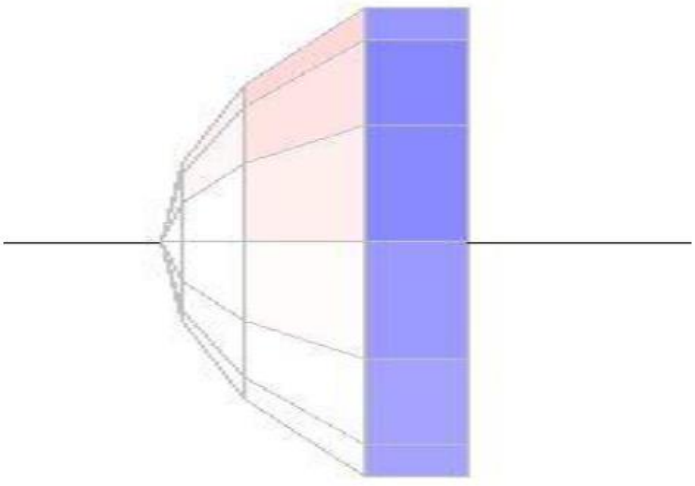

Figure 12. Lens with a negative plano-convex shape in 3D.

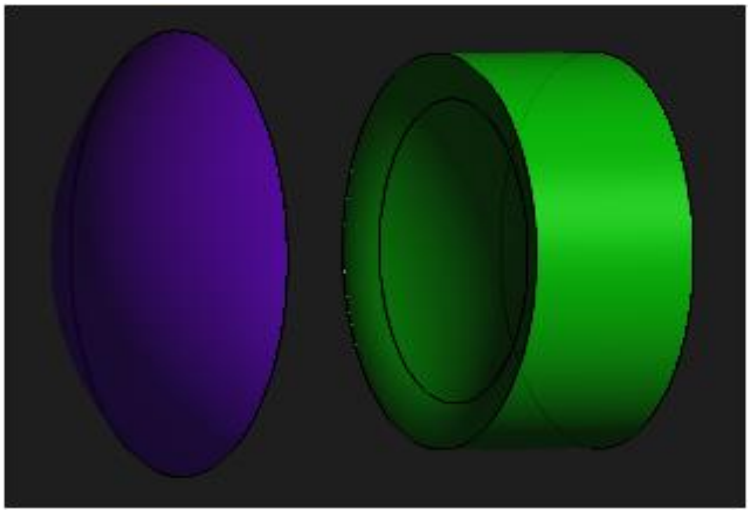

Figure 13. Glass lens 3D model from opt cad solid work.

The third stage involves using a vertical lathe and a cutting cylinder with a diameter restricted by the lens's dimensions to remove the lens glass from the raw mold. Figure 14 shows a real-life photo of a glass material being sliced.

Figure 14. Real image of cutting from glass material to proposed lens array.

The fourth and last phase in the lens-making process is the sculpting using a glass-made hard-abrasive stone specifically developed for the purpose. As long as the water is flowing, the carved surface will not be scratched, therefore this is an important feature to have. Figure 15, 16 depicts these operations.

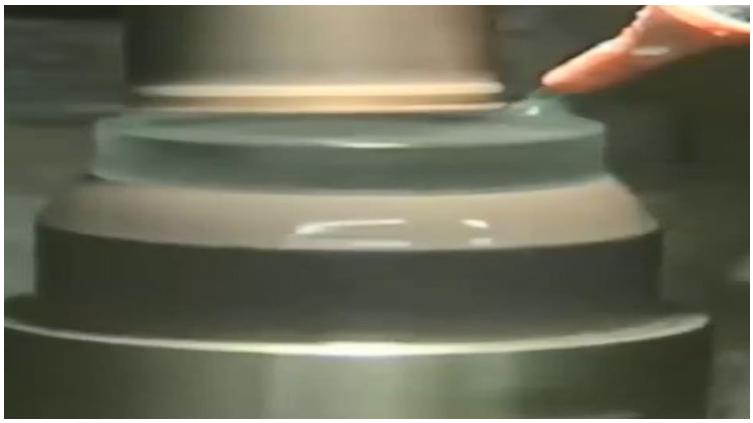

Figure 15. Sculpting operation of lens.

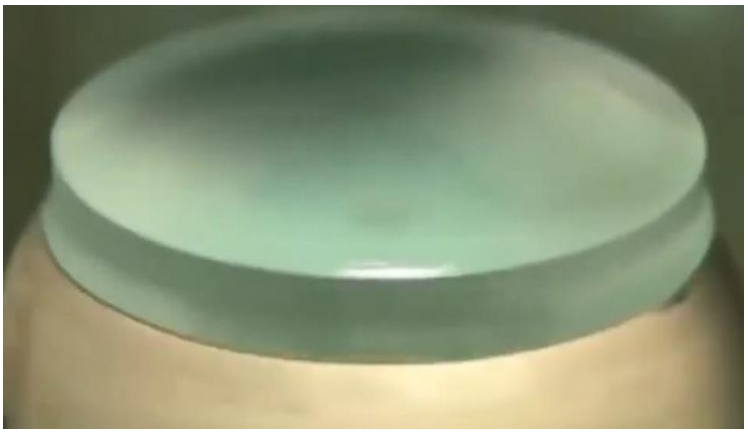

Figure 16. Lens after sculpting process.

Taking the Fifth Step In order to ensure that the lens sticks to the metal surface of the polishing machine, an asphalt material must be applied to its surface before it can be placed in the machine. Figure 17, 18 shows this operation. Indicated in figure 19. polishing metal curving surfaces and lens images, and then putting them both together.

Figure 17. The process of adding asphalt.

Figure 18. Lens after putting in the polishing machine.

Figure 19. Lens after putting the metal curved surface.

The layout of optical lenes positive and negative in Figure 20, and 21.

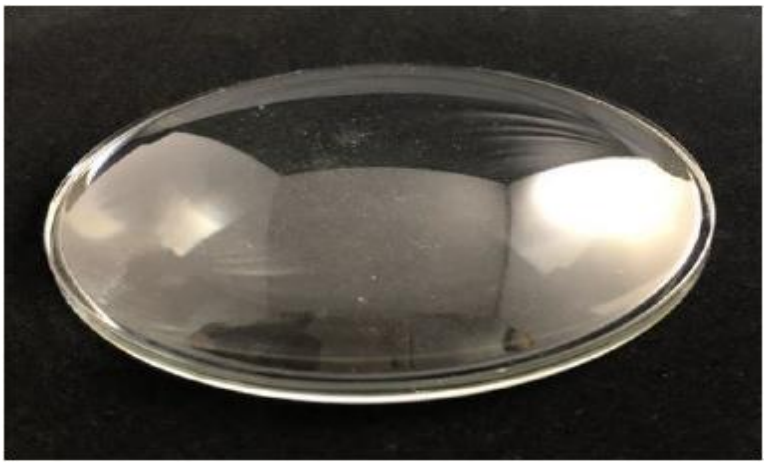

Figure 20. The real 3D design of a positive plano-convex lens after polishing.

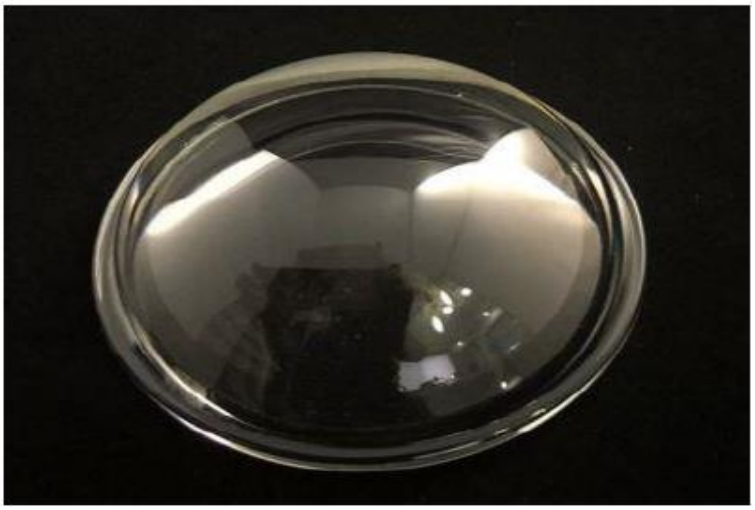

Figure 21. The real 3D design of a negative plano-convex lens after polishing.

The 3D positive and negative lens holder deign by solid work given by figure 22.

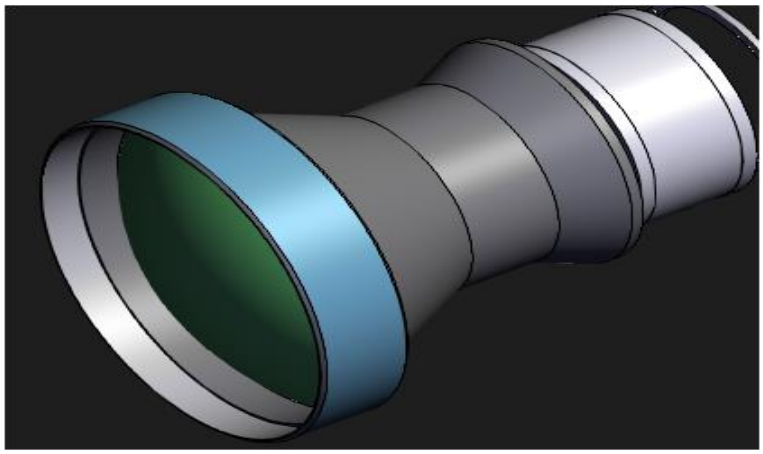

Figure 22. 3D model of a holder lenses by solid work.

The real image of chamber test of high-power fiber laser shown in figure 23.

Figure 23. The hardware implementation of CTHPF.

4. The Test Result

The chamber is vacuumed to a pressure of 0.01 atm, nitrogen gas is compressed to keep moisture out, and then the pressure is restored to its original value. Finally, an optical power meter with an optical attenuator is used to protect the optical power meter's sensor to measure the laser beam's power. Figure 24 depicts what I'm talking about. Show all the experiment components at once.

1470 watts of output power have been measured. There is a letter-shaped connection (T) attached to the vacuum pump's inlet side to allow air to enter the chamber and the aerosol tank to be regularly inserted. After these steps, the evacuation pump's function is reversed to assist in pumping air into the chamber and allowing aerosol to enter the chamber. When we discover the relationship between the metal sheet's heat capacity and the laser beam's temperature.

The heat capacity is inversely related to the number of particles circulating inside the chamber, as we'll see in the results. When we reduce the number of particles in the chamber test, we receive the following results in figures 25 and 26: absorption and scattering values. T and HC have a relationship, as shown. Metal sheet's heat capacity increases when T from laser beams increases to melting point, and metal sheet melts. The melting point difference between steel and aluminum sheets is 800°C to 1100°C in the former and 400°C to 600°C in the latter. Two samples of stainless steel and aluminum exposed to a laser beam from the chamber test are shown in real life in Figures (27 to 30). in table2. summarized the importance result of heat capacity with laser beam temperature.

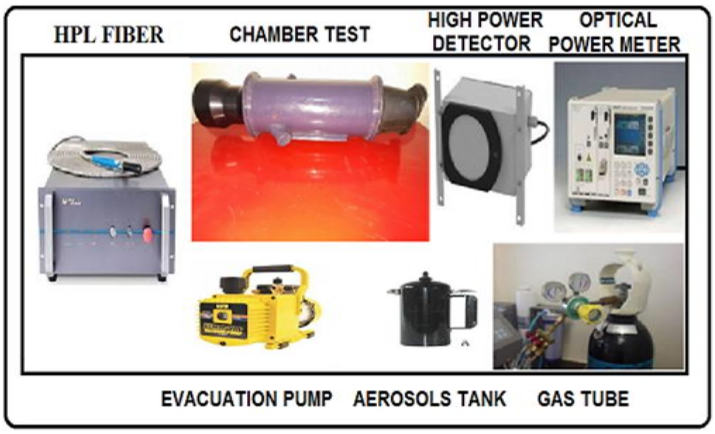

Figure 24. Real image of experiment components.

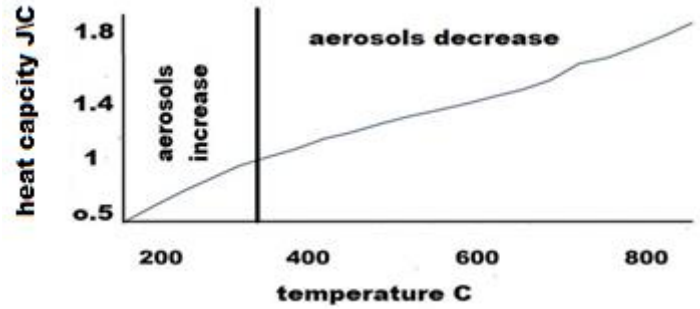

Figure 25. Relation between heat capacity and temperature for aluminum sheet metal.

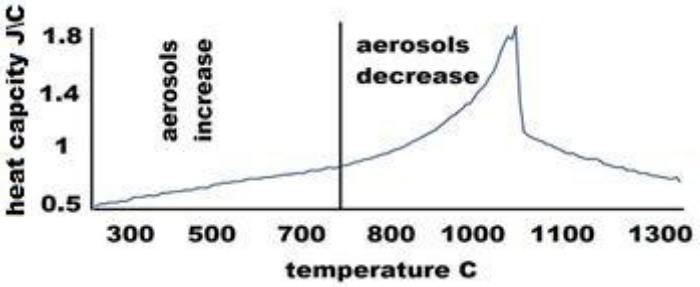

Figure 26. Relation between heat capacity and temperature for stainless steel.

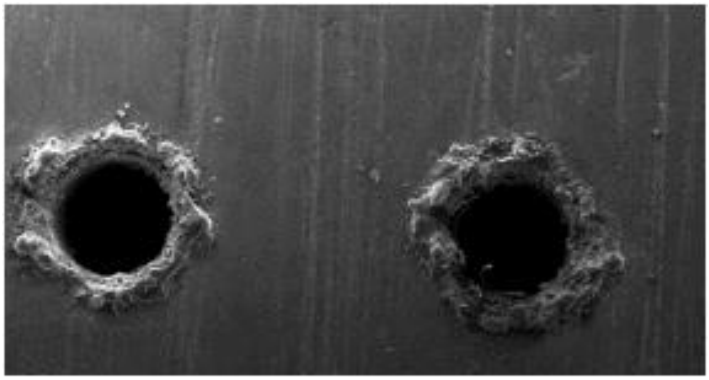

Figure 27. The real image of steel after aerosols decreases.

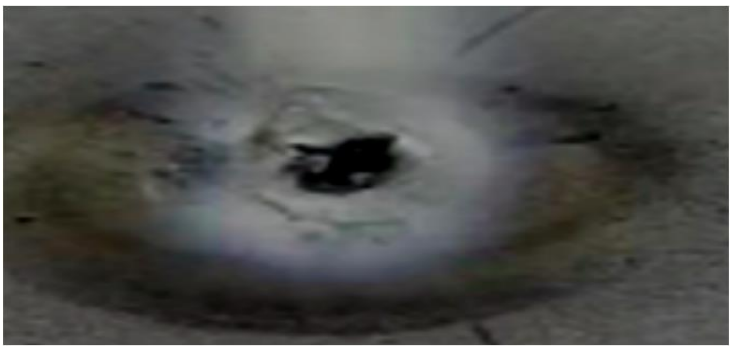

Figure 28. The real image of steel after aerosols increases.

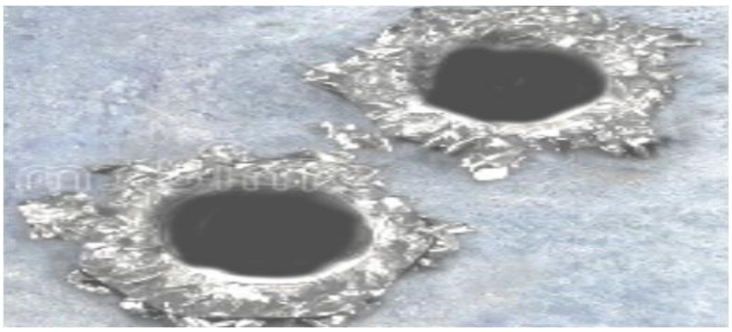

Figure 29. The real image of aluminum after aerosols decreases.

Figure 30. The real image of aluminum after aerosols increases.

Table 2. summarized the importance values of heat capacity with laser beam temperature for aluminum and stainless-steel

Aluminum heat capacity	**Laser beam temperature**	**Stainless-steel Heat capacity**	**Laser beam temperature**
0.5 J\C	200 C	0.5 J\C	300 C
1 J\C	400 C	1 J\C	800 C
1.4 J\C	600 C	1.4 J\C	1000 C
1.8 J\C	800 C	1.8 J\C	1050 C

5. Conclusion

In order to pass and collect the laser beam, two Plano convex lenses are used in the high-power fiber laser chamber test. The vacuum pump, aerosol tank and nitrogen gas inlet are located on the seats in this room. This weather simulation system works flawlessly. In order to test the high-power laser module, the proposed system designed a simple technology to expose it to an aerosol and see how it affects different types of sheet metal, such as aluminum and stainless steel. Pre-use in a real application the lab gives designers a chance to test their products before they go into the field. The results showed that by increasing the aerosol in the case of interaction between the laser beam and each of the following metals, aluminum and stainless steel, the temperature of the laser beam decreases significantly with the heat capacity. These values, in order from HC, are equal to 1.4 J/C. We find that the temperature of the beam reaches 200 C and in the second case of stainless steel is 700 C.

References

1. Mohamed, A. A., Ahmed, M., Hamed, H. F., Shehata, M., Elsawi, A. R., & Almslmany, A. (2021, July). Design and Implementation of Absorption and Scattering Chamber Test of a High-Power Fiber Laser Beam by Gases and Solids in the Far-Field. *In 2021 International Telecommunications Conference (ITC-Egypt)* (pp. 1-4). IEEE.
2. Daigle, Jean-François, Grégoire Tremblay, Francis Théberge, and Dominik Pudo. The importance of thermal blooming for laser weapon atmospheric propagation modelling. *In Propagation Through and Characterization of Atmospheric and Oceanic Phenomena*, pp. PTh2E-4. Optical Society of America, 2021.
3. Chamankhah, Shahram, Mohsen Bazargan, Ali Forouzandeh, and Siavash Riahi. Feasibility Study of Fracture Propagation Controlled by Use of Managed Pressure Drilling during Laser-Assisted Drilling Operation. *SPE Journal (*2021): 1-12.
4. Danson, Colin N., Constantin Haefner, Jake Bromage, Thomas Butcher, Jean-Christophe F. Chanteloup, Enam A. Chowdhury, Almantas Galvanauskas et al. Petawatt and exawatt class lasers worldwide. *High Power Laser Science and Engineering 7* (2019).
5. Sprangle, P., Ting, A., Penano, J., Fischer, R., & Hafizi, B. (2008). Incoherent combining and atmospheric propagation of high-power fiber lasers for directed-energy applications. *IEEE Journal of quantum electronics*, 45(2), 138-148.
6. Kienle, Alwin, et al. Spatially resolved absolute diffuse reflectance measurements for noninvasive determination of the optical scattering and absorption coefficients of biological tissue. *Applied optics* 35.13 (1996): 2304-2314.
7. Miles, Rachael EH, Antonia E. Carruthers, and Jonathan P. Reid. Novel optical techniques for measurements of light extinction, scattering and absorption by single aerosol particles. *Laser & Photonics Reviews* 5.4 (2011): 534-552.
8. Grismayer, Thomas, et al. Laser absorption via quantum electrodynamics cascades in counter propagating laser pulses. *Physics of Plasmas* 23.5 (2016): 056706.
9. Pinton, Gianmarco, et al. Attenuation, scattering, and absorption of ultrasound in the skull bone. *Medical physics* 39.1 (2012): 299-307.
10. Svanberg, Sune. Optical analysis of trapped gas—gas in scattering media absorption spectroscopy. *Laser Physics* 20.1 (2010): 68-77.
11. Bindhu, C. V., et al. Laser propagation and energy absorption by an argon spark. *Journal of Applied Physics* 94.12 (2003): 7402-7407.
12. Fazio, E., et al. Nonlinear scattering and absorption effects in size-selected diphenylpolyynes. *The Journal of Physical Chemistry* C 118.49 (2014): 28812-28819.
13. Hajjarian, Zeinab, and Seemantini K. Nadkarni. Correction of optical absorption and scattering variations in laser speckle rheology measurements. *Optics express* 22.6 (2014): 6349-6361.
14. Lundberg, Johan, et al. Light tracking through ice and water—Scattering and absorption in heterogeneous media with PHOTONICS. *Nuclear Instruments and Methods in Physics Research Section A: Accelerators, Spectrometers, Detectors and Associated Equipment* 581.3 (2007): 619-631.
15. Müller, Markus G., et al. Intrinsic fluorescence spectroscopy in turbid media: disentangling effects of scattering and absorption. *Applied Optics* 40.25 (2001): 4633-4646.
16. Jacques, Steven L., and Scott A. Prahl. Modeling optical and thermal distributions in tissue during laser irradiation. *Lasers in surgery and medicine* 6.6 (1987): 494-503.
17. Akue Asseko, André Chateau, et al. Thermal modeling in composite transmission laser welding process: light scattering and absorption phenomena coupling. *Key Engineering Materials.* Vol. 611. *Trans Tech Publications Ltd*, 2014.
18. Gratton, Enrico, et al. Measurements of scattering and absorption changes in muscle and brain. *Philosophical Transactions of the Royal Society of London. Series B: Biological Sciences* 352.1354 (1997): 727-735.
19. Spangle, P., Hafizi, B., Ting, A., & Fischer, R. (2015). High-power lasers for directed-energy applications. *Applied optics*, 54(31), F201-F209.
20. Jhajj, N., Rosenthal, E. W., Birnbaum, R., Wahlstrand, J. K., & Milchberg, H. M. (2014). Demonstration of long-lived high-power optical waveguides in air. *Physical Review* X, 4(1), 011027.
21. . Chamankhah, Shahram, Mohsen Bazargan, Ali Forouzandeh, and Siavash Riahi. Feasibility Study of Fracture Propagation Controlled by Use of Managed Pressure Drilling during Laser-Assisted Drilling Operation. SPE Journal (2021): 1-12.

22. Yang, L., & Miklavcic, S. J. (2005). Theory of Light Propagation incorporating scattering and absorption in turbid media. *Optics letters*, 30(7), 792-794.
23. Wei, Y., Ma, L., Cao, T., Zhang, Q., Wu, J., Buseck, P. R., & Thompson, J. E. (2013). Light scattering and extinction measurements combined with laser-induced incandescence for the real-time determination of soot mass absorption cross section. *Analytical chemistry*, 85(19), 9181-9188.
24. Brunner, H., Mayer, A., & Sussner, H. (1972). Resonance Raman scattering on the haem group of oxy-and deoxyhaemoglobin. *Journal of molecular biology*, 70(1), 153-156.
25. Gray, D. R., & Kilkenny, J. D. (1980). The measurement of ion acoustic turbulence and reduced thermal conductivity caused by a large temperature gradient in a laser heated plasma. *Plasma Physics*, 22(2), 81.
26. Tran, H. C., Lo, Y. L., & Huang, M. H. (2017). Analysis of scattering and absorption characteristics of metal powder layer for selective laser sintering. *IEEE/ASME Transactions on Mechatronics*, 22(4), 1807-1817.
27. Jeong, Y. C., Boyland, A. J., Sahu, J. K., Chung, S. H., Nilsson, J., & Payne, D. N. (2009). Multi-kilowatt single-mode ytterbium-doped large-core fiber laser. *Journal of the Optical Society of Korea*, 13(4), 416-422.
28. Gondarenko, A., Levy, J. S., & Lipson, M. (2009). High confinement micron-scale silicon nitride high Q ring resonator. *Optics express*, 17(14), 11366-11370.